Chi-Pu Lin
Department of Civil and Environmental Engineering,
University of Washington,
Seattle, WA 98195
e-mail: cpl7@uw.edu

Richard Wiebe
Department of Civil and Environmental Engineering,
University of Washington,
Seattle, WA 98195
e-mail: rwiebe@uw.edu

Kao-Hao Chang[1]
Department of Civil Engineering,
Chung Yuan Christian University,
Taoyuan 320314, Taiwan;
Department of Civil Engineering,
National Kaohsiung University of Science and Technology,
Kaohsiung 807618, Taiwan
e-mail: khchang@cycu.edu.tw

Static Response of Circular Cavities With a Non-Radial Crack Subject to Antiplane Stress

Tunnels, pipelines, and other subterranean circular cavities are common components of modern infrastructure. In addition, seismic activities are common in many areas with pipelines, which may put these structures under unknown risk of fracture. A particular risk case of interest can be characterized as a plane strain problem with a circular cavity and crack in an infinite plane under antiplane stress. Antiplane, i.e., mode III, loading has seen less study relative to modes I and II due to the lower risk factor in structures that are especially vulnerable to fracture (e.g., in the automotive and aerospace industries), and the increase in complexity compared to modes I and II. The work here further explores this phenomenon on circular cavities, and particularly, the effect of non-radial cracks on the stress intensity factor via a parametric study. The study introduces a semi-analytical method and also uses commercial finite element software to further expand on the investigation.
[DOI: 10.1115/1.4056430]

Keywords: stress intensity factor, crack opening displacement, antiplane stress, mode III, XFEM, elasticity, stress analysis

1 Introduction

Subterranean structures, e.g., tunnels and pipelines, in earthquake-prone regions may undergo complex cyclic loading leading to cracking. Comprehensive knowledge of the local stress field around the crack tip is crucial for analyzing and designing resilient subterranean structures that do not fail catastrophically in the presence of small cracks (or small subsurface defects in materials).

There have been extensive studies on the static Stress Intensity Factor (SIF) of cracks near/embedded in circular cavities dating back to the 1960 s. However, there has been less focus on the case of antiplane (i.e., mode III) loading due to the lower risk factor associated with structures particularly vulnerable to fractures (e.g., in the aerospace and automotive industries). This is not the case for subterranean structures, as mentioned before. Additionally, mode III problems are more complex than modes I and II as they require full three-dimensional (3D) models. Although antiplane shear deformations are sometimes considered to be simple to model mathematically, it is essential to capture the corresponding out-of-plane behavior to understand the cavity–crack interaction. As such, the work presented here will focus on the SIF of circular cavities with an embedded non-radial crack under antiplane loading by using a semi-analytical method and a Finite Element (FE) model developed with commercial software. In this sense, an embedded non-radial crack is one for which the orientation of the crack is not (necessarily) perpendicular to the surface of the circular cavity. This can be contrasted with much of the prior work which focused on radial cracks.

The overarching goals of this work are to (1) present a semi-analytical method that calculates the mode III SIF, which is compared against results from previous studies, and (2) explore the efficacy/difficulties of FE for mode III problems. As mentioned before, there is a relative lack of work on FE mode III problems, which the authors aim to address. The FE models are employed in a parametric study to look at the effects of size and orientation of the cavity/crack on the SIF. The study looks at (1) the validity of using a 3D FE model to capture a theoretically infinite body problem, (2) the validity of a 2D model to capture non-orthogonal loading, and (3) the limitations of each model.

1.1 Background. This subsection will briefly discuss previous work on the SIF of cracks. Relevant analytical work will be discussed, followed by numerical studies.

1.1.1 Previous Analytical Studies. In general, exact solutions are strictly limited to certain geometries and loading conditions. Those antiplane shear problems concerning cavities with edge cracks are very rare, albeit simple at first glance. For a single axial crack (or two collinear axial cracks, i.e., one on either side of the cavity) attached to the rim of the elliptical cavity, to the authors' knowledge, the very first elegant expressions of mode III SIFs date back to the early 1970 s when they were derived via continuous dislocations [1,2]. Note that an axial crack is regarded as a case of a radial crack. Subsequently, the utilization of integral transforms leads to the same closed-form expressions [3]. For a circular cavity with two collinear radial cracks, the mode III SIF can be derived in explicit and concise form using the complex variable method [4]. In addition, Rice [5,6] provided an exact linear elastic-perfectly plastic solution for an edge crack in a finite-width plane. A general solution was available for a sharp notch (or, as a limiting case, a crack) considering any relation between stress and strain in the work-hardening range [6,7]. Beyond this, the authors are not aware of other benchmark solutions available for comparison.

1.1.2 Previous Numerical Studies. There have also been several numerical studies on the SIF of cracks. The Finite Element Method (FEM) is a widely used numerical tool in engineering and has also been extensively employed in fracture mechanics problems (other numerical methods, e.g., boundary element methods, have also been used but are not the focus of this paper). Finite element methods for modeling cracks in commercial software can be mostly divided into two categories: (1) local mesh refinement near the crack tip, and (2) eXtended Finite Element Method (XFEM). This discussion will focus on the latter as it is the method used in the FE model herein and has been widely adopted to model fracture mechanics problems.

[1]Corresponding author.

Contributed by the Applied Mechanics Division of ASME for publication in the Journal of Applied Mechanics. Manuscript received October 9, 2022; final manuscript received December 3, 2022; published online January 6, 2023. Assoc. Editor: Pradeep Sharma.

The main advantage of the XFEM is it does not require the crack to align with the vertices of the elements; i.e., the mesh does not need to conform to the crack. This is immediately beneficial when investigating crack growth as the model does not require remeshing after the crack propagates. Similarly, it becomes advantageous in the case of a parametric study where the size and orientation of the crack are variable, but the mesh can remain consistent and relatively coarse around the crack tip. The XFEM achieves this by using a displacement field approximation that can model an arbitrary discontinuity and the near-tip asymptotic crack fields. It was first introduced in Refs. [8,9], in which it was shown that discontinuous functions can be used with the partition of unity concept—presented in Ref. [10]—to enrich finite element approximations; the method showed promising results for solving geometric discontinuous problems such as cracks.

Since the introduction of XFEM, numerous studies using the method for fracture mechanics problems followed. Nagashima et al. looked at the SIF of structures with a crack between dissimilar materials with XFEM [11]. It was also used to look at fracture in composite materials in 2D and 3D examples which produced accurate results of the mechanics of an interface crack in Ref. [12]. Furthermore, Javanmardi and Maheri introduced a new algorithm for predicting crack initiation and growth direction in 3D solid concrete using an anisotropic damage-plasticity model and XFEM; they compared the model against three benchmark examples with experimental data and were found to be in good agreement [13]. Similarly, Roth et al. [14] presented a novel 3D plain concrete XFEM cracking model to look at the structural stability of large structures (with emphasis on concrete dams); they demonstrated good agreement with benchmark problems available from the literature and direct application for real industrial structures. Zhuang et al. [15] showed an example illustrating antiplane crack propagation in a plate using XFEM with the crack growth path being linear as expected.

There has also been considerable work done on improving the XFEM for SIF calculations. Liu et al. [16] introduced a new XFEM formulation that enriches the crack tip fields using higher-order terms of the crack tip asymptotic field and found that it resulted in excellent agreement with analytical and numerical results in the literature. Areias and Belytschko [17] presented a new formulation and a numerical procedure for XFEM to analyze 3D crack propagation in brittle and quasi-brittle solids. In addition, Shen and Lew [18] introduced a variant of the XFEM to optimize convergence using a discontinuous Galerkin method.

For a discussion on—and comparison between—different FEM fracture modeling approaches for linear elastic fracture mechanic problems, the reader is referred to Ref. [19]. Moreover, for an in-depth overview of the XFEM and its application, the reader is referred to Ref. [20].

1.2 Scope.

The work presented here will focus on the static SIF of an infinite body with a circular cavity and an embedded crack using the semi-analytical method and the XFEM. The semi-analytical method, which is exact for an infinite domain, is used to test the accuracy of the FEM. Thereafter, the FEM is used to explore the range of validity of the infinite-domain assumption for finite domain problems and other limitations of the semi-analytical formulation (namely the semi-analytical method is limited to cavities with radial cracks). A study focused on optimizing the XFEM is beyond the scope of this work, as the goal at this stage was an accurate truth model, and not necessarily the fastest model.

The following sections will discuss both the semi-analytical method and the numerical model. Furthermore, the results using the semi-analytical method and the numerical model will be validated against previous work in the literature for both SIF and crack opening displacement (COD). In addition, the setup and results for the parametric study will be discussed, followed by the findings on the validity of using 2D or 3D models for different cavity–crack problems.

2 Semi-Analytical Method

This section will discuss the formulation of the semi-analytical method used in the study presented here. Discussions on the FEM and validation of the models with results in the literature are given in Sec. 2.1.

Consider an infinitely large matrix, containing a zero-thickness radial crack attached at the rim of a circular cavity, as depicted in Fig. 1. The matrix is subjected to uniform antiplane loading τ^{∞} (at an arbitrary angle α, i.e., angle of loading) in the far field (extending to infinity r^{∞}). The unbounded matrix is assumed to be homogeneous, isotropic, and linearly elastic. The length of the crack and the radius of the cavity are a and b, respectively. The full-plane material has the shear modulus μ. The crack tip is taken as the origin of global polar coordinates (r, θ). The origin of local polar coordinates (r_1, θ_1) is set at the center of the cavity.

Introducing an auxiliary boundary S_a of circular shape, the whole plane is divided into two regions: an open region 1 and an enclosed region 2 (Fig. 1). In these two regions, the only non-vanishing out-of-plane components of the displacements u_j have to obey the governing Laplace equations, namely

$$\frac{1}{r}\frac{\partial}{\partial r}\left(r\frac{\partial u_j}{\partial r}\right)+\frac{1}{r^2}\frac{\partial^2 u_j}{\partial \theta^2}=0, \quad j=1,2 \tag{1}$$

where the subscript j denotes the region number.

The stress-free boundary conditions are imposed on the surface of the cavity and expressed in terms of the polar coordinates

$$\tau^{(1)}_{r_1 z}=\mu\frac{\partial u_1(r_1,\theta_1)}{\partial r_1}=0, \quad -\pi\le\theta_1\le\pi, \quad r_1=b \tag{2}$$

Accordingly, the zero-stress boundary conditions are enforced on the crack edge (i.e., the top and bottom faces of the crack) and written in terms of polar coordinates (r, θ)

$$\tau^{(2)}_{\theta z}=\frac{\mu}{r}\frac{\partial u_2(r,\theta)}{\partial \theta}=0, \quad \theta=\pm\pi, \quad 0\le r\le a \tag{3}$$

2.1 Eigenfunction Expressions.

For the present boundary-value problem, the use of the method of eigenfunction expansions is effective. This idea benefits from Westergaard's function and Williams' series because these explicit expressions describe the near-tip stress and displacement fields [21–23], Considering the full-plane medium without any anomalies, the free-field displacement u^F under remote shear loads may be expressed as

$$u^F(r,\theta)=\frac{\tau^{\infty}}{\mu}r\cos(\theta-\alpha) \tag{4}$$

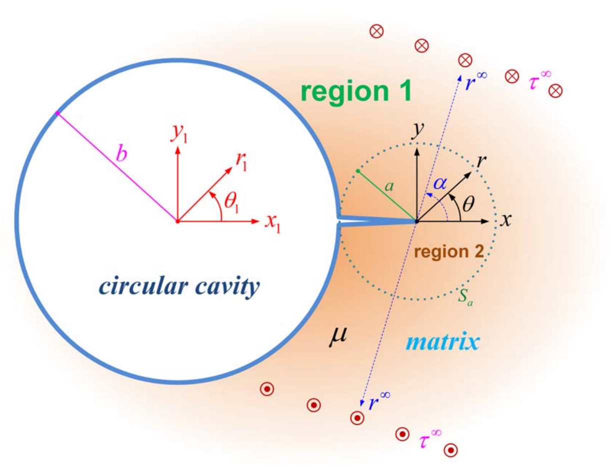

Fig. 1 Geometric layout of a circular cavity with a radial crack

The "total" perturbed displacement field u^P in open region 1 may be separated into two parts: u^{P1} and u^{P2}. Thus,

$$u^P = u^{P1} + u^{P2} \tag{5}$$

The first component u^{P1} represents the perturbed displacement field due to the effect of region 2

$$u^{P1}(r, \theta) = A_0 \ln\left(\frac{r}{a}\right) + \sum_{n=1}^{\infty} A_n \left(\frac{a}{r}\right)^n \cos(n\theta) + \sum_{n=1}^{\infty} B_n \left(\frac{a}{r}\right)^n \sin(n\theta) \tag{6}$$

where the expansion coefficients A_0, A_n, and B_n are unknown.

The second component u^{P2} indicates the perturbed displacement field induced by the existence of the cavity. Following Eq. (6), we may write

$$u^{P2}(r_1, \theta_1) = C_0 \ln\left(\frac{r_1}{b}\right) + \sum_{n=1}^{\infty} C_n \left(\frac{b}{r_1}\right)^n \cos(n\theta_1) + \sum_{n=1}^{\infty} D_n \left(\frac{b}{r_1}\right)^n \sin(n\theta_1) \tag{7}$$

where the expansion coefficients C_0, C_n, and D_n are unknown which will be solved in Sec. 2.3.

In region 1, the resultant displacement field u_1, which is composed of the free field and the total perturbed field, is given by

$$u_1 = u^F + u^P \tag{8}$$

In region 2, the displacement field u_2 that satisfies Eqs. (1) and (3) is given by

$$u_2(r, \theta) = \sum_{n=0}^{\infty} E_n \left(\frac{r}{a}\right)^n \cos(n\theta) + \sum_{n=0}^{\infty} F_n \left(\frac{r}{a}\right)^{\frac{2n+1}{2}} \sin\left(\frac{2n+1}{2}\theta\right) \tag{9}$$

where the expansion coefficients E_n and F_n will be determined later. Notice that Eq. (9) inherently possesses the inverse square root stress singularity at the crack tip.

2.2 Coordinate Transformation.

When imposing the continuity conditions on S_a, unifying the two distinct polar coordinate systems in regions 1 and 2 is indispensable. The coordinate transformation relations from the start coordinate (r_s, θ_s) to the end coordinate (r_e, θ_e) are recast in an appropriate form as

$$r_s = \Upsilon(r_e, \theta_e) = [r_e^2 + 2(s-e)(a+b)r_e \cos\theta_e + (a+b)^2]^{1/2} \tag{10}$$

$$\theta_s = \Theta(r_e, \theta_e) = \tan^{-1}\left[\frac{r_e \sin\theta_e}{r_e \cos\theta_e + (s-e)(a+b)}\right] \tag{11}$$

Details are available in Appendix A.

Making use of Eqs. (10) and (11), we may rewrite Eq. (7) in terms of (r, θ) as

$$u^{P2}(r, \theta) = C_0 \ln\left[\frac{\Upsilon(r, \theta)}{b}\right] + \sum_{n=1}^{\infty} C_n \left[\frac{b}{\Upsilon(r, \theta)}\right]^n \cos[n\Theta(r, \theta)] + \sum_{n=1}^{\infty} D_n \left[\frac{b}{\Upsilon(r, \theta)}\right]^n \sin[n\Theta(r, \theta)] \tag{12}$$

Similarly, when applying Eq. (2) to the cavity surface, we may rewrite Eq. (6) in terms of (r_1, θ_1) as

$$u^{P1}(r_1, \theta_1) = A_0 \ln\left[\frac{\Upsilon(r_1, \theta_1)}{a}\right] + \sum_{n=1}^{\infty} A_n \left[\frac{a}{\Upsilon(r_1, \theta_1)}\right]^n \cos[n\Theta(r_1, \theta_1)] + \sum_{n=1}^{\infty} B_n \left[\frac{a}{\Upsilon(r_1, \theta_1)}\right]^n \sin[n\Theta(r_1, \theta_1)] \tag{13}$$

2.3 Determination of Expansion Coefficients.

Across the artificial interface S_a, we enforce the stress continuity condition

$$\tau_{rz}^{(1)}(r, \theta) = \tau_{rz}^{(2)}(r, \theta), \quad -\pi \le \theta \le \pi, \quad r = a \tag{14}$$

and the displacement continuity

$$u_1(r, \theta) = u_2(r, \theta), \quad -\pi \le \theta \le \pi, \quad r = a \tag{15}$$

Multiplying Eqs. (14) and (15) by a succession of cosine functions and integrating over the range $[-\pi, \pi]$ leads to

$$\int_{-\pi}^{\pi} \frac{\partial u_1(a, \theta)}{\partial r} \cos(q\theta) d\theta = \int_{-\pi}^{\pi} \frac{\partial u_2(a, \theta)}{\partial r} \cos(q\theta) d\theta, \quad q = 0, 1, \ldots, \tag{16}$$

$$\int_{-\pi}^{\pi} u_1(a, \theta) \cos(q\theta) d\theta = \int_{-\pi}^{\pi} u_2(a, \theta) \cos(q\theta) d\theta, \quad q = 0, 1, \ldots \tag{17}$$

Likewise, invoking Eq. (2) produces

$$\int_{-\pi}^{\pi} \frac{\partial u_1(b, \theta_1)}{\partial r_1} \cos(q\theta) d\theta = 0, \quad q = 0, 1, \ldots \tag{18}$$

Going further with the aid of the property of orthogonal basis functions, and reducing Eqs. (16)–(18), the following relations hold

$$A_n = 0, \quad n = 0, 1, \cdots \tag{19}$$

$$C_0 = C_n = 0, \quad n = 2, 3, \cdots \tag{20}$$

$$C_1 = \frac{\tau^{\infty}}{\mu} b \cos\alpha \tag{21}$$

$$E_n = \delta_{1,n} \frac{\tau^{\infty}}{\mu} a \cos\alpha + \frac{\varepsilon_n I_n^c}{2\pi}, \quad n = 0, 1, \cdots \tag{22}$$

with

$$I_n^c = bC_1 \int_{-\pi}^{\pi} \cos\frac{[\Theta(a, \theta)]}{\Upsilon(a, \theta)} \cos(n\theta) d\theta, \quad n = 0, 1, \ldots \tag{23}$$

where $\delta_{1,n}$ denotes the Kronecker delta function and ε_n is the Neumann factor, which is 1 if $n = 0$ and 2 if $n \ge 1$.

Subsequently, we proceed analogously. Multiplying Eqs. (2), (14), and (15) by a sequence of sine functions, integrating, and exploiting the orthogonality conditions gives the two relations below

$$D_n = \delta_{1,n} \frac{\tau^{\infty}}{n\mu} b \sin\alpha + \frac{b}{n\pi} \sum_{p=1}^{\infty} B_p I_{p,n}^{s1} \tag{24}$$

$$F_n = \frac{2}{\pi(2n+1)} \left\{ \frac{\tau^{\infty}}{\mu} a \sin\alpha I_{1,n}^s - \sum_{p=1}^{\infty} pB_p I_{p,n}^s + a \sum_{p=1}^{\infty} D_p \hat{I}_{p,n}^{s2} \right\} \tag{25}$$

and also yields a system of linear algebraic equations for unknown coefficients B_n

$$\sum_{n=0}^{\infty} B_n K_{q,n} = H_q, \quad q = 0, 1, \ldots \tag{26}$$

Detailed expressions are given in Appendix B (Eqs. (B1)–(B6)).

From a computational point of view, truncating the infinite series in Eqs. (24)–(26) to a finite number of terms is needed. The expansion coefficients B_n may be evaluated by standard matrix techniques. In Eq. (26), the summation indices n and the weighting indices q are truncated after $N-1$ terms. Therefore, Eq. (26) constitutes a system of N equations with N unknowns. The number of truncation terms considered depends only on the required accuracy.

Once the coefficients B_n are found, the expansion coefficients D_n and F_n can be straightforwardly evaluated *via* Eqs. (24) and (25).

2.4 Near-Tip Stress Field. From Eq. (9), we may obtain the radial stress around the cusped point of the crack. Clearly, the dominant singularity arises in the leading term of the second infinite sum when the radial distance r approaches zero. Hence, the near-tip stress field is given by

$$\lim_{r\to 0} \tau_{rz}^{(2)}(r,\theta) \sim \frac{\mu}{2\sqrt{r}} F_0 \sin\frac{\theta}{2} \tag{27}$$

Based on linear elastic fracture mechanics, we may introduce the stress intensity factor K_3

$$K_3 = \lim_{r\to 0} \sqrt{2\pi r}\, \tau_{rz}^{(2)}(r,\ \theta) \tag{28}$$

For later comparison, it is convenient to define the following normalized SIF:

$$K_{III} = \frac{K_3}{\tau^\infty \sqrt{\pi L_c} \sin\alpha} \tag{29}$$

where L_c is the chosen length. One may specify L_c using the exact solution or reference solution available in the literature. For example, L_c is the "half" crack length [4] for the case of a single finite crack, while L_c is the "full" crack length [24] or the sum of the cavity radius and the full crack length [3] for the case of cavity-crack interaction.

2.5 Convergence Test. Since the present semi-analytical solution is expressed in series form, a few convergence tests are performed to find a sufficient number of truncation terms. Based on some numerical experiments, the suitable truncation value N gradually goes up when the length of the crack increases. For example, $N = 120$ is adequate for $a/b < 0.5$ and $N = 135 \sim 150$ for $1 < a/b < 1.5$ to produce reliable results.

2.6 Finite Element Model. To compare the results from the semi-analytical method, in addition to results in the literature, a numerical model was developed using ABAQUS, a commercial (general purpose) FE software. Moreover, the numerical model also serves as a tool to extend beyond the limitations of the semi-analytical model in the parametric study (discussed later), as well as investigate the validity of using a 3D or 2D model for different types of cavity-crack problems.

The FE model is a cube with length (l), width (w), and height (h) of 40 m. The cavity is located in the center of the cube, and the crack is modeled using XFEM (the crack was not allowed to grow); the radius of cavity b and the length of the crack a are variables. In the case where the cavity is omitted, the crack is then located at the center of the cube instead. A study on the boundary effects, i.e., the model size needed to converge to the solution of an infinite-domain assumption, is discussed later in Sec. 5.3.

Figure 2 shows a diagram of the FE model and the boundary condition/loading used. The model uses approximately 405,246 nodes and 186,561 elements (3D 8-node reduced integration brick elements; C3D8R in ABAQUS), varying depending on the radius of the cavity. A preliminary mesh size study was undertaken to determine the nominal element and cube size required. In addition to the boundary condition in Fig. 2, all nodes are pinned in the x and y directions to simulate a pure antiplane shear problem; this was observed to produce the most accurate SIF calculations when compared to exact solutions. The SIFs were observed from the mid-width of the cube, i.e., at $z = w/2$.

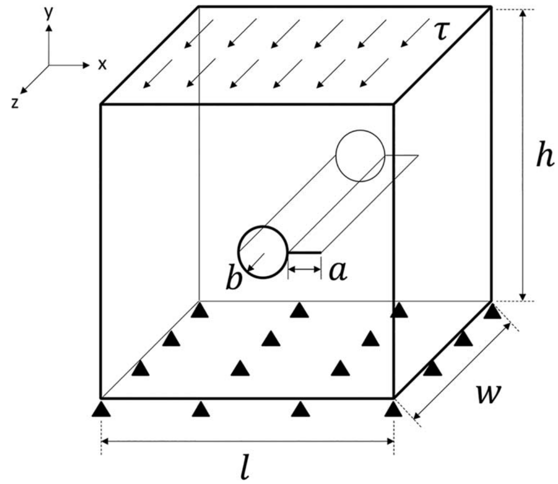

Fig. 2 Diagram of XFEM model

3 Validation Against Benchmark Results

This section discusses the validation of the semi-analytical and numerical models. The validation is split into four parts: (1) the crack opening displacement of a straight crack; (2) the SIF of a straight crack with varying angle of loading α; (3) the SIF of a single straight crack embedded in a circular cavity with varying ratios of $(a+b)/b$; and (4) the SIF of a single non-radial crack embedded in a circular cavity with varying ratios of $(a+b)/b$.

3.1 Crack Opening Displacement. The exact solution of the COD for a straight crack (i.e., $b = 0$) in an infinite plate is given by the Westergaard stress function, shown in Refs. [21,25], as follows:

$$\Delta u(c) = \frac{2\tau^\infty}{\mu} \operatorname{Im}\left(\sqrt{c^2 - \left(\frac{a}{2}\right)^2}\right) \tag{30}$$

where c is the position with respect to the mid-crack location. Figure 3 shows the plot of the COD with $\tau^\infty = 1000$ MPa, $\mu = 80,000$ MPa, and $a = 2$ mm. As shown in the figure, the results from the models are in good agreement.

3.2 Stress Intensity Factor of a Crack With Varying Angle of Loading. For the SIF, Sih [4] obtained closed-form solutions for

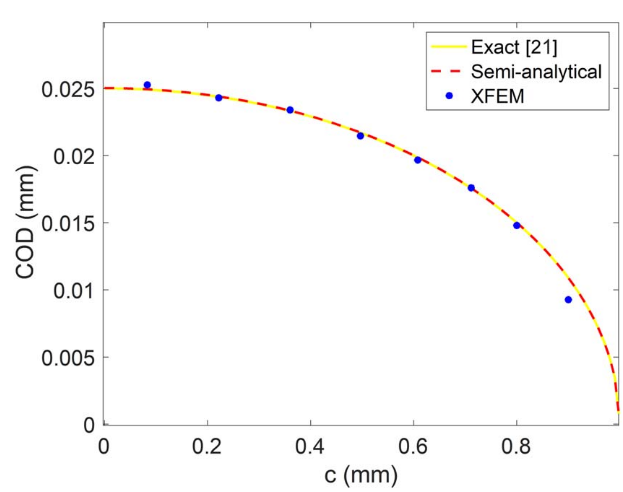

Fig. 3 Crack opening displacement of straight crack

the SIF of a crack in an infinite body under antiplane shear at an angle of loading α—shown in the denominator in Eq. (29). Figure 4 is the plot of the normalized SIF with varying angles of loading. As shown in the figure, the results from the models are in good agreement.

3.3 Stress Intensity Factor of a Straight Crack Embedded in a Cavity. Table 1 gives some computed results of the normalized SIF with $(a+b)/b = 1.5$, 2.0, 2.5, 3.0, 3.5, and 4.0, respectively. To reveal the accuracy of the present semi-analytical and FE solutions, the calculated results of the exact solution, obtained from Eqs. (2) and (11) in Ref. [3], are also included in Table 1. Good consistency exists between the present results and those of Ref. [3]. Clearly, these results ensure that the formulism presented in Sec. 2 is effective.

3.4 Stress Intensity Factor of a Non-Radial Crack Embedded in a Cavity. Isida and Tsuru [24] applied the body force method to evaluate the SIF of a non-radial crack embedded in a circular cavity/inclusion. Figure 5 shows a plot of the normalized SIF for a crack embedded in a cavity at 45 deg from the x-axis. As noted before, the semi-analytical results are not provided as it is limited to radial cracks. Again, the results from the models are in good agreement.

As shown in the figures of this subsection, the FE models can calculate the COD and SIF for single cracks with varying angles of loading, and non-radial cracks imbedded in a circular cavity. The following section will generalize the case to include variable a/b, angle of loading, and orientation of the crack in a parametric study.

4 Parametric Study

It has been shown in the literature that the ratio of the size of the crack and cavity, a/b, affects the SIF, as well as the angle of loading. The parameters shown thus far are sufficient to characterize the problem for a cavity with a radial crack. The angle of the crack relative to the horizontal direction, β, see Fig. 6, is used to generalize the problem to non-radial cracks.

4.1 Parametric Study Results. Figure 7 includes plots of the normalized SIFs of the parametric study. The top left subplot is a 3D scatter plot of a/b equal to 0.5, 1.0, and 2.0. The remaining three subplots are the color plots for the three a/b values. Similarly to the results from Ref. [3], the SIFs were normalized using Eq. (29) with; however, α is substituted with β because the orientation of the crack relative to the angle of loading is given by β. As shown in the figure, the normalized SIF in smaller a/b is more sensitive to changes in α and β. Interestingly, the normalized SIF does not necessarily increase with the a/b ratio (similar findings were shown in Ref. [3]); for bigger a/b, the normalized SIF increases for large α and small β, and decreases for small α and large β. Note that when $\alpha = \beta$, the problem collapses to the particular case of a radial crack. Thus, from the gradient of the case with a radial crack (i.e., $\alpha = \beta$), the normalized SIF is not sensitive to either α or β, as expected.

Figure 8 shows the same results as Fig. 7 but without normalizing the SIF. Table 2 provides the parameters used for Fig. 8, with $\tau^\infty = 10$ MPa and $b = 2$ mm. Interestingly, the SIF is almost symmetrical about a 45-deg line for $a/b = 0.5$. For example, the SIF when $\alpha = 60$

Table 1 Values of the normalized SIF

$(a+b)/b$	Semi-analytical	XFEM	Exact (Tweed and Melrose, 1989)
1.5	0.8784	0.8683	0.8783
2.0	0.9186	0.9185	0.9185
2.5	0.9073	0.8987	0.9073
3.0	0.8889	0.8891	0.8889
3.5	0.8712	0.8681	0.8712
4.0	0.8558	0.8567	0.8558

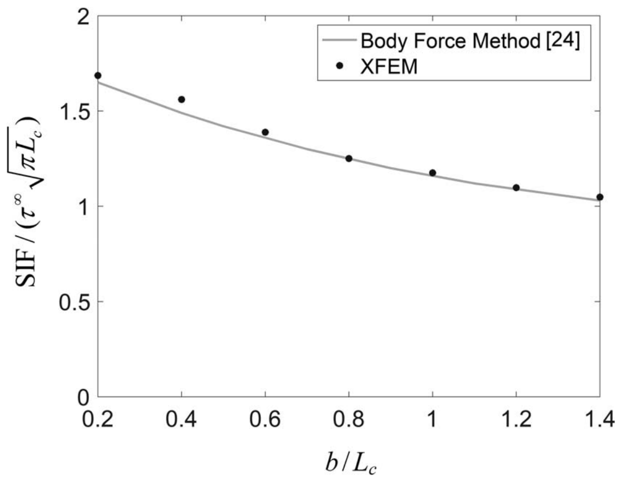

Fig. 5 SIF of crack embedded in a circular cavity

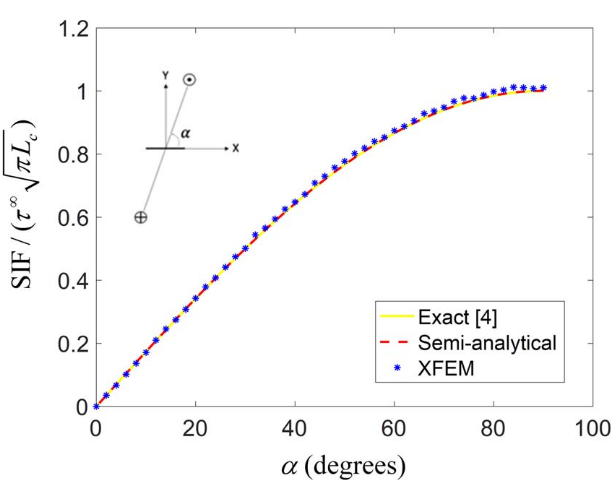

Fig. 4 SIF of crack with varying angle of loading

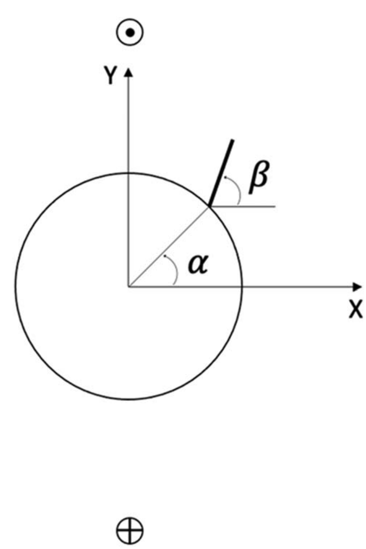

Fig. 6 Orientation of crack and angle of loading

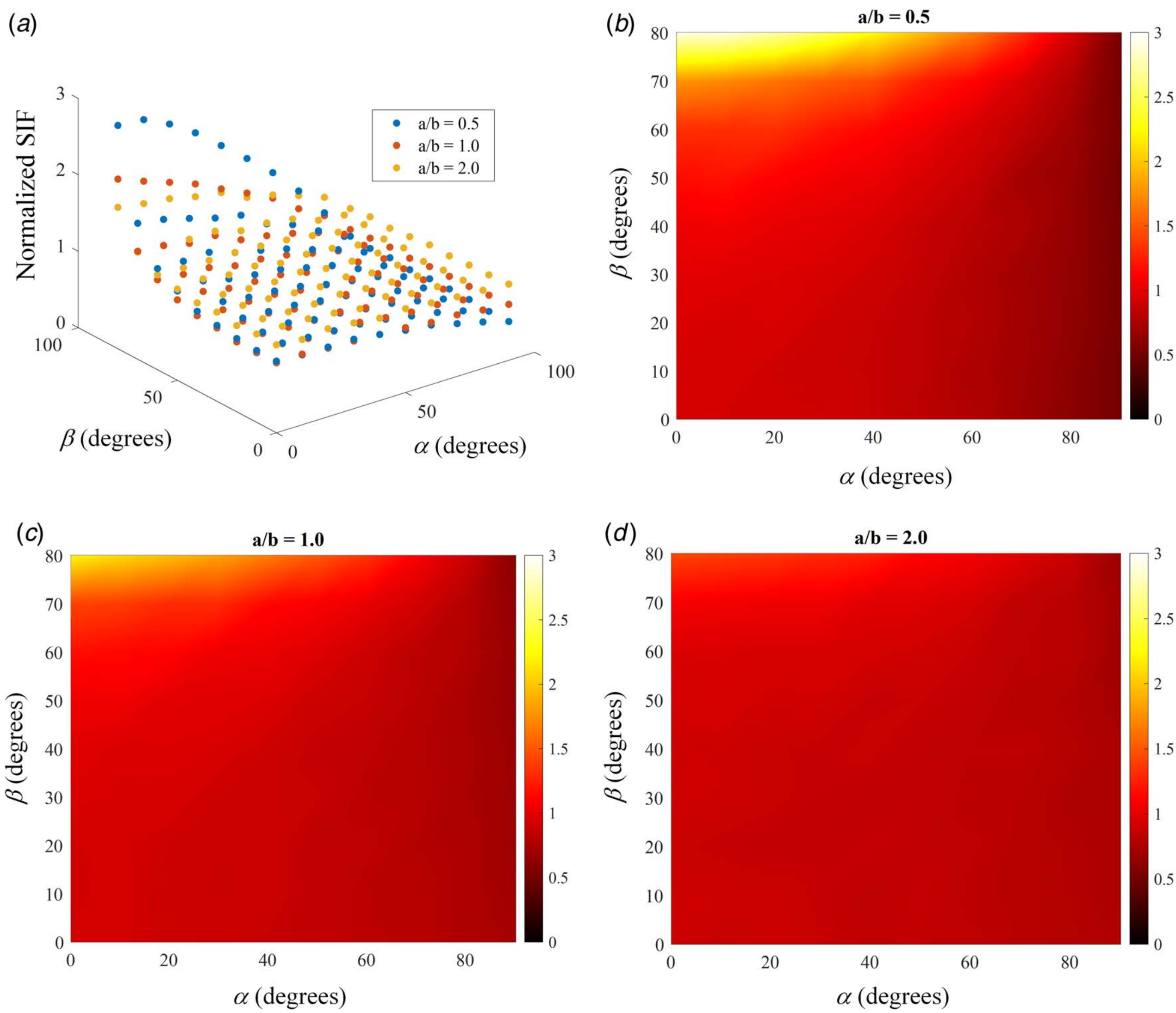

Fig. 7 Normalized SIFs of a non-radial crack in a circular cavity: (*a*) 3D scatter plot for $a/b = 0.5$, 1.0, and 2.0, (*b*)–(*d*) planimetric shaded relief plots for $a/b = 0.5$, 1.0, and 2.0, respectively.

and $\beta = 0$ deg is similar to that of $\alpha = 0$ and $\beta = 60$ deg. On the contrary, when $a/b = 2$ there is no symmetry and the SIF becomes sensitive to β and not to α. This indicates that the cavity is more critical to the SIF at lower a/b, whereas the crack is more critical to the SIF at higher a/b, which is as expected.

4.2 Range of Validity. Three-dimensional FE models can solve general crack problems but are computationally expensive and may encounter issues such as boundary condition effects when solving theoretical infinite-domain problems. Two-dimensional analytical models, on the other hand, are not computationally expensive but may be limited to a few particular cases (e.g., orthogonal loading). This subsection explores the suitability and accuracy of 2D and 3D models by looking at (1) the boundary effects on the 3D XFEM model—using various model sizes for a constant cavity and crack size; (2) non-orthogonal loading and how accurately 2D models can find mode III SIF; and (3) what the normalized SIF approaches as crack length increases (relative to cavity radius) and the a/b required to approach the asymptotic value.

4.2.1 Boundary Effects on Three-Dimensional Finite Element Model. To evaluate the boundary effects on the 3D FE model, a cavity with an embedded non-radial crack ($\alpha = 0$, $\beta = 45$ deg) with $a/b = 1$ is explored. The length (l), height (h), and width (w) of the FE model, see Fig. 2, are varied but the mesh density is kept constant. Table 3 shows the percent error of the different size FE models, which keeps two dimensions constant and varies the third dimension. Notably, the width—i.e., dimension along the z-direction—does not have a significant impact on the accuracy of the SIF. The SIF is most sensitive to the length parameter, as expected. In order to obtain good results, the width, height, and length should be approximately 4, 5, and 10 times $(a + b)$.

4.2.2 Two-Dimensional Model for Non-Orthogonal Loading. As mentioned previously, the full 3D FE model is able to capture modes I, II, and III SIF for cases of non-orthogonal loading. In order to evaluate the accuracy of the 2D model in capturing 3D problems (Fig. 9), the mode III SIF of the 3D XFEM model is compared against the mode III SIF of the 2D analytical model (single straight crack without cavity). Note that the loading for the 2D model is the z-component of the loading of the 3D model. In addition, every node was pinned in the y-direction (i.e., the x-direction pin was removed). Table 4 shows the SIFs of the 2D and 3D models, which are in good agreement. This indicates that the 3D problem can be modeled separately using 2D models by taking the orthogonal components (i.e., modes I, II, and III), which is as expected with the principle of superposition. While the results appear to be obvious or trivial, this study has not been conducted before, to the extent of the authors' knowledge, and is worth exploring with XFEM.

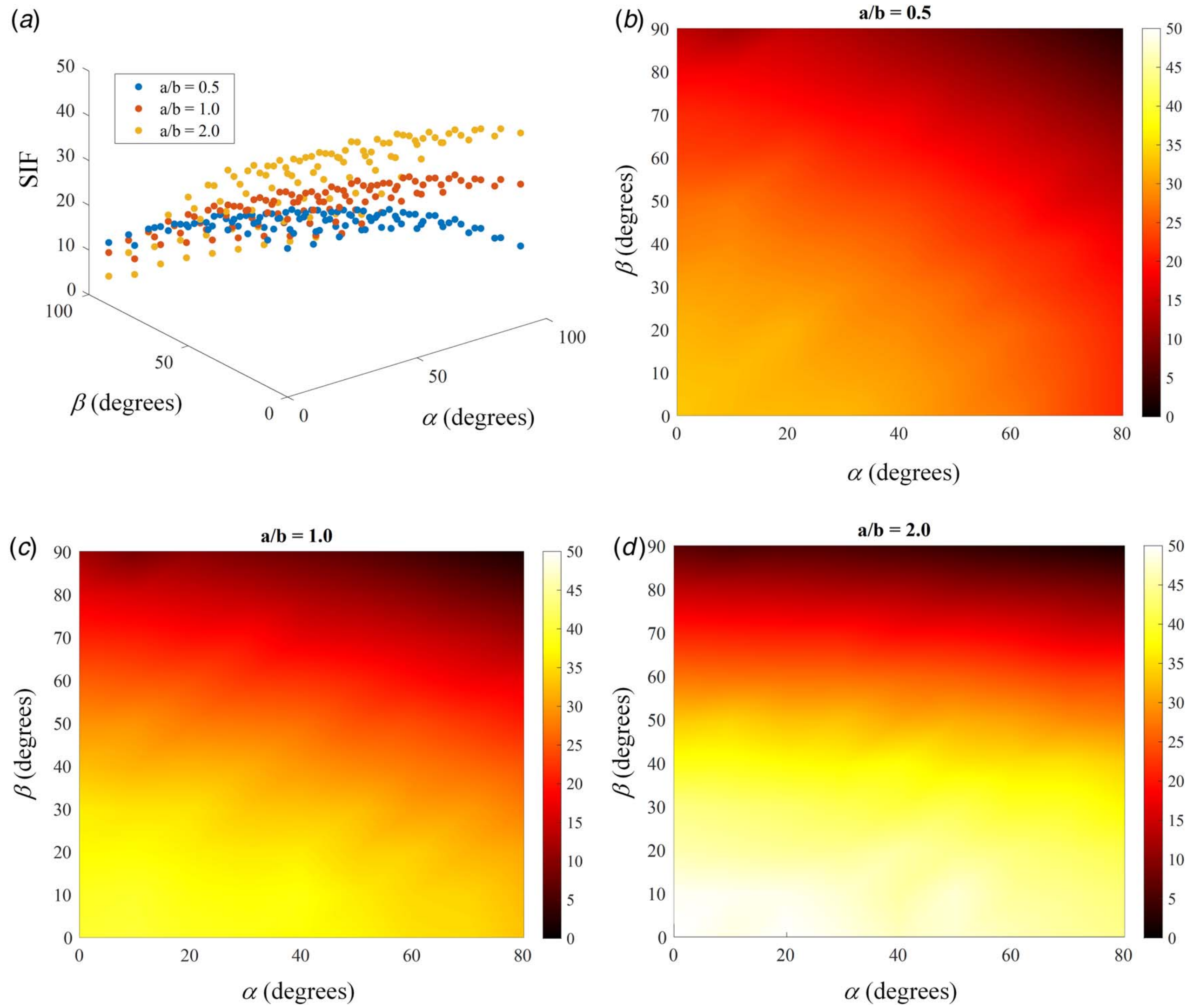

Fig. 8 SIFs of a non-radial crack in a circular cavity: (*a*) 3D scatter plot for *a/b* = 0.5, 1.0, and 2.0, (*b*)–(*d*) planimetric shaded relief plots for *a/b* = 0.5, 1.0, and 2.0, respectively

Table 2 Parameters for SIF with non-radial crack

a/b	*a*
0.5	2 mm
1.0	4 mm
2.0	8 mm

4.2.3 Upper Bound of the Cavity Effect. Due to the computational cost of the 3D FE model, it is useful to know the crack length relative to the cavity size that corresponds to the normalized SIF approaching the asymptotic value. The ability to utilize the 3D FE model does not depend on the absolute size of the crack and cavity but instead on the crack length relative to the radius of the cavity. For example, if the crack and cavity are similar in size, the size of the model can be adjusted to accommodate an

Table 3 SIF With varying model sizes

Length change		Height change		Width change	
$\frac{h}{a+b}=\frac{w}{a+b}=10$		$\frac{l}{a+b}=\frac{w}{a+b}=10$		$\frac{h}{a+b}=\frac{l}{a+b}=10$	
$\frac{l}{a+b}$	% Error	$\frac{h}{a+b}$	% Error	$\frac{w}{a+b}$	% Error
10	1.13	10	1.13	10	1.13
7.5	4.27	7.5	1.66	8.415	1.22
5	5.88	5	0.98	6.83	1.39
2.5	27.81	2.5	9.29	5.245	2.87
–	–	–	–	3.66	2.51
–	–	–	–	2.075	5.85
–	–	–	–	1.4375	5.68

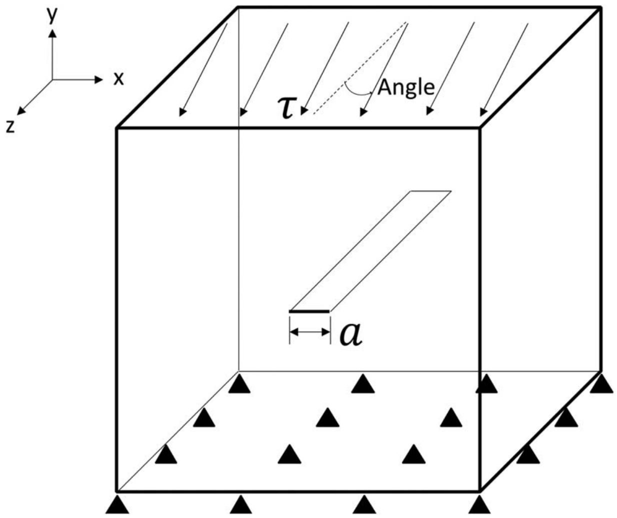

Fig. 9 Non-orthogonal loading

Table 4 2D and 3D Mode III SIF for non-orthogonal loading

Angle (deg)	3D FE	(Sih, 1963)	% Difference
0	25.74	25.07	2.69
26.57	23.02	22.42	2.68
45.00	18.20	17.72	2.68

appropriate mesh density. However, if the crack is much bigger than the cavity (or vice versa), then the total number of elements required in order to model the cavity and crack would be impractical.

From Eqs. (2) and (11) in Ref. [3], it is calculated that the normalized SIF asymptotically approaches 0.701 as $(a+b)/b$ tends to infinity. Furthermore, the upper bound of the normalized SIF is 0.9186 with $(a+b)/b$ approximately equal to 2. To get within 90% of 0.701 (i.e., 0.736), the crack length and cavity radius would need to be 10 times the cavity radius. The $(a+b)/b$ increases to 24 and 740 to get within 95 and 99%, respectively.

5 Conclusion

A semi-analytical method was introduced to treat cavity-crack interaction problems under antiplane loading. Both COD and SIF are provided in a series solution. As a consequence of the singular nature of eigenfunctions that enclose the crack, low computational requirements allow for fast exploration of initial trial calculations and parametric studies, with minimal matrix manipulations.

To further explore more general cavity–crack problems, an XFEM model was developed. A parametric study was conducted to look at the effects of the size, location, and orientation of the cavity and crack; the following are the pertinent findings:

(1) The normalized SIF in smaller a/b is more sensitive to changes in α and β. The opposite is true for SIF (not normalized).
(2) The normalized SIF does not necessarily increase with bigger a/b. For big α and small β, the normalized SIF increases with bigger a/b. For small α and big β, the normalized SIF decreases with bigger a/b.
(3) The SIF is more sensitive to changes to α for lower a/b.

A study was conducted to look at the validity of using 2D or 3D models for different types of problems. For 3D FE models attempting to solve infinite body mode III problems, the width of the model does not have much impact on the accuracy of the SIF. The SIF is most sensitive to the length of the model. For accurate results, the width, height, and length should be approximately 4, 5, and 10 times $(a+b)$, respectively. In addition, it was shown that a cavity and crack under a non-orthogonal load can be resolved into the orthogonal components and solved individually with a 2D model.

For future work that can improve upon the study, the semi-analytical method can be generalized to solve problems that include non-radial cracks, inclusions, multiple cracks, and gaps between the cavity and crack. Further work is also needed to expand this study into the dynamic response from antiplane shear waves.

Acknowledgment

The authors would like to thank John and Wen Su for their generous contributions. The opinions presented herein are solely those of the authors.

Funding Data

- This research is supported by the John and Wen Su Term Research Acceleration Fund, and also by Su Development.

Conflict of Interest

There are no conflicts of interest.

Data Availability Statement

The authors attest that all data for this study are included in the paper.

Appendix A

When the polar coordinate (r_1, θ_1) is to be rewritten in terms of (r, θ), the start coordinate (r_s, θ_s) and the end coordinate (r_e, θ_e) are regarded as (r_1, θ_1) and (r_0, θ_0), respectively. This implies that the subscripts s and e are taken as 1 and 0, respectively. Based on Eqs. (10) and (11), we have

$$r_1 = \Upsilon(r, \theta) = [r^2 + 2(a+b)r\cos\theta + (a+b)^2]^{1/2} \tag{A1}$$

$$\theta_1 = \Theta(r, \theta) = \tan^{-1}\left[\frac{r\sin\theta}{r\cos\theta + (a+b)}\right] \tag{A2}$$

Appendix B

In Eqs. (24)–(26), the pertinent functions are listed as follows:

$$I^{s1}_{p,n} = -pa^p \int_{-\pi}^{\pi} \frac{\sin[p\Theta(b, \theta_1)]}{\Upsilon(b, \theta_1)^2} \frac{\Upsilon'(b, \theta_1)}{\Upsilon(b, \theta_1)^{p-1}} \sin(n\theta_1) d\theta_1 \tag{B1}$$

$$I^{s}_{p,n} = \frac{8p(-1)^{p-n}}{(2n+1)^2 - (2p)^2} \tag{B2}$$

$$\hat{I}^{s2}_{p,n} = -pb^p \int_{-\pi}^{\pi} \frac{\sin[p\Theta(a, \theta)]}{\Upsilon(a, \theta)^2} \frac{\Upsilon'(a, \theta)}{\Upsilon(a, \theta)^{p-1}} \sin\left(\frac{2n+1}{2}\theta\right) d\theta \tag{B3}$$

$$K_{q,n} = \frac{2n}{\pi} \sum_{p=0}^{\infty} \frac{I^s_{n,p} I^s_{p,q}}{2p+1} - \pi\delta_{q,n} - \frac{b}{\pi} \sum_{p=1}^{\infty} \frac{I^{s1}_{n,p} I^{s2}_{p,q}}{p} + \frac{2ab}{\pi^2} \sum_{p=0}^{\infty} \frac{I^s_{p,q}}{2p+1} \sum_{j=1}^{\infty} \frac{I^{s1}_{n,j} \hat{I}^{s2}_{j,p}}{j} \tag{B4}$$

$$H_q = \frac{\tau^\infty}{\mu}\sin\alpha\left[\delta_{1,q}\pi a + b\sum_{p=1}^{\infty}\frac{\delta_{1,p}}{p}\hat{I}^{s2}_{p,q} - \frac{2a}{\pi}\sum_{p=0}^{\infty}\frac{I^s_{1,p}I^s_{p,q}}{2p+1} - \frac{2ab}{\pi}\sum_{p=0}^{\infty}\frac{I^s_{p,q}}{2p+1}\left(\sum_{j=1}^{\infty}\frac{\delta_{1,j}}{j}\hat{I}^{s2}_{j,p}\right)\right] \tag{B5}$$

$$I^{s2}_{p,q} = b^p\int_{-\pi}^{\pi}\frac{\sin\left[p\Theta(a,\theta)\right]}{\Upsilon(a,\theta)^p}\sin(q\theta)d\theta \tag{B6}$$

where the primes stand for differentiation with respect to the arguments of corresponding functions.

References

[1] Yokobori, T., Kamei, A., and Konosu, S., 1971, "Report of Research Institute for Strength and Fracture of Materials," Tohoku University, Sendai, Japan, **7**, p. 57.

[2] Yokobori, T., Ichikawa, M., Konosu, S., and Takahashi, R., 1972, "Report of Research Institute for Strength and Fracture of Materials," Tohoku University, Sendai, Japan, **8**, p. 1.

[3] Tweed, J., and Melrose, G., 1989, "Cracks at the Edge of an Elliptic Hole in Out of Plane Shear," Eng. Fract. Mech., **34**(3), pp. 743–747.

[4] Sih, G. C., 1963, "Stress-Intensity Factors for Longitudinal Shear Cracks," AIAA J., **1**(10), pp. 2387–2388.

[5] Rice, J. R., 1966, "Contained Plastic Deformation Near Cracks and Notches Under Longitudinal Shear," Int. J. Fract. Mech., **2**(2), pp. 426–447.

[6] Rice, J. R., 1968, "Mathematical Analysis in the Mechanics of Fracture," *Fracture: An Advanced Treatise*, 2nd ed., H. Liebowitz, ed., Academic Press, New York, pp. 191–311.

[7] Rice, J. R., 1967, "Stresses Due to a Sharp Notch in a Work Hardening Elastic-Plastic Material Loaded by Longitudinal Shear," ASME J. Appl. Mech., **34**(2), pp. 287–298.

[8] Belytschko, T., and Black, T., 1999, "Elastic Crack Growth in Finite Elements With Minimal Remeshing," Int. J. Numer. Methods Eng., **45**(5), pp. 601–620.

[9] Moës, N., Dolbow, J., and Belytschko, T., 1999, "A Finite Element Method for Crack Growth Without Remeshing," Int. J. Numer. Methods Eng., **46**, pp. 131–150.

[10] Melenk, J., and Babuška, I., 1996, "The Partition of Unity Finite Element Method: Basic Theory and Applications," Comput. Methods Appl. Mech. Eng., **39**(1–4), pp. 289–314.

[11] Nagashima, T., Omoto, Y., and Tani, S., 2003, "Stress Intensity Factor Analysis of Interface Cracks Using X-FEM," Comput. Methods Appl. Mech. Eng., **56**(8), pp. 1151–1173.

[12] Huynh, D. B. P., and Belytschko, T., 2009, "The Extended Finite Element Method for Fracture in Composite Materials," Int. J. Numer. Methods Eng., **77**(2), pp. 214–239.

[13] Javanmardi, M. R., and Maheri, M. R., 2019, "Extended Finite Element Method and Anisotropic Damage Plasticity for Modelling Crack Propagation in Concrete," Finite Elem. Anal. Des., **165**, pp. 1–20.

[14] Roth, S.-N., Léger, P., and Soulaïmani, A., 2020, "Strongly Coupled XFEM Formulation for Non-planar Three-Dimensional Simulation of Hydraulic Fracturing With Emphasis on Concrete Dams," Comput. Methods Appl. Mech. Eng., **363**, p. 112899.

[15] Zhuang, Z., Liu, Z., Cheng, B., and Liao, J., 2014, *Extended Finite Element Method*, Elsevier Science and Technology, Waltham, MA, p. 137.

[16] Liu, X. Y., Xiao, Q. Z., and Karihaloo, B. L., 2004, "XFEM for Direct Evaluation of Mixed Mode SIFs in Homogeneous and Bi-materials," Int. J. Numer. Methods Eng., **59**(8), pp. 1103–1118.

[17] Areias, P. M. A., and Belytschko, T., 2005, "Analysis of Three-Dimensional Crack Initiation and Propagation Using the Extended Finite Element Method," Int. J. Numer. Methods Eng., **63**(5), pp. 760–788.

[18] Shen, Y., and Lew, A., 2010, "An Optimally Convergent Discontinuous Galerkin-Based Extended Finite Element Method for Fracture Mechanics," Int. J. Numer. Methods Eng., **82**(6), pp. 716–755.

[19] Marco, M., Infante-García, D., Belda, R., and Giner, E., 2020, "A Comparison Between Some Fracture Modelling Approaches in 2D LEFM Using Finite Elements," Int. J. Fract., **223**(1–2), pp. 151–171.

[20] Fries, T.-P., and Belytschko, T., 2010, "The Extended/Generalized Finite Element Method: An Overview of the Method and Its Applications," Int. J. Numer. Methods Eng., **84**(3), pp. 253–304.

[21] Westergaard, H. M., 1939, "Bearing Pressures and Cracks: Bearing Pressures Through a Slightly Waved Surface or Through a Nearly Flat Part of a Cylinder, and Related Problems of Cracks," ASME J. Appl. Mech., **6**(2), pp. pp. A49–A53.

[22] Williams, M. L., 1957, "On the Stress Distribution at the Base of a Stationary Crack," ASME J. Appl. Mech., **24**(1), pp. 109–114.

[23] Williams, M. L., 1952, "Stress Singularities Resulting From Various Boundary Conditions in Angular Corners of Plates in Extension," ASME J. Appl. Mech., **19**(4), pp. 526–528.

[24] Isida, M., and Tsuru, H., 1981, "A Circular Inclusion and an Arbitrary Array of Cracks in Infinite Body Under Antiplane Shear," Trans. Jpn. Soc. Mech. Eng., Ser. A, **47**(420), pp. 810–817.

[25] Tada, H., Paris, P. C., and Irwin, G. R., 2000, *The Stress Analysis of Cracks Handbook*, 3rd ed., ASME Press, New York.